RSC Advances

PAPER

View Article Online
View Journal | View Issue

Cite this: *RSC Adv.*, 2024, **14**, 9497

Physical properties of ferromagnetic Mn-doped double perovskites (DPs) $Cs_2AgInCl/Br_6$ for spintronics and solar cell devices: DFT calculations

N. A. Noor, *[a] Wasim Tahir, [b] Sohail Mumtaz [c] and Hosam O. Elansary[d]

A computational framework based on density functional theory (DFT) has been effectively employed to investigate the wide-ranging physical characteristics of ferromagnetic manganese (Mn)-substituted double perovskites (DPs) with composition $Cs_2AgIn_{1-x}Mn_xCl/Br_6$ (x = 0.0, 0.25). This research covers a systematic exploration of the mentioned DPs for potential applications in the domains of spintronics and energy conversion devices. The physics concerning ferromagnetic (FM) $Cs_2AgIn_{0.75}Mn_{0.25}Cl/Br_6$ DPs was studied computationally using the modified Becke–Johnson (mBJ-LDA) potential and the generalized gradient approximation (PBEsol GGA) method introduced by Perdew, Burke, and Ernzerhof. The structural, electronic, magnetic, and transport behavior of materials were investigated using these computations. Structural parameters for both perovskite materials were computed subsequent to their optimization in FM phase. According to evaluations of the electronic band structure and density of states (DOS), the incorporation of Mn ions into the host lattice causes exchange splitting induced by p–d hybridization, consequently stabilizing the FM state. Probing the sharing of magnetic moment, charge, and spin between the substituent cations and the host anions led to the comprehensive elaboration of this exchange splitting of bands. Important parameters such as exchange constants ($N_0\alpha$, $N_0\beta$), and direct spin-exchange splitting Δ_x(d), support the stability of the FM state. Finally, we briefly explored the spin effect on other aspects of electronic transport, the Seebeck coefficient, and the power factor, using the conventional Boltzmann transport theory.

Received 29th January 2024
Accepted 11th March 2024

DOI: 10.1039/d4ra00754a

rsc.li/rsc-advances

1. Introduction

During the recent past, perovskite nano-crystals with chemical composition ($APbX_3$, where A = Cs^{1+}, $CH(NH_2)_2^{1+}$, $CH_3NH_3^{1+}$; X = Br^{1-}, Cl^{1-}, I^{1-}) have attracted significant interest from the materials science community because of their outstanding optical characteristics. Owing to their appealing optoelectronic features, these materials are frequently used in numerous devices, including solar cells, photo-detectors, and light emitting diodes (LEDs).[1,2] However, the main issue impeding the usage of lead halide perovskites is their lower stability over prolonged light exposure, high temperature, or humidity. In addition, lead's toxicity and bioaccumulation in the environment present another problem. These challenges are currently provoking materials scientists to search for new stable, ecologically friendly metal halide perovskite NCs having analogous optoelectronic characteristics.[3–9] In this context, the replacement of toxic lead (Pb^{2+}) ions with other not much toxic divalent cations of IV-group of the periodic table (*i.e.* Sn^{2+}, Ge^{2+}) can be the best possible approach to develop lead-free halides.[10–14] But the observed conversion of the oxidation state from divalent (Sn^{2+}, Ge^{2+}) configuration to tetravalent (Sn^{4+}, Ge^{4+}) configuration, puts a question mark on the stability of these halides. Fortunately, this dilemma is finely addressed by material researchers through the substitution of two divalent lead (Pb^{2+}) cations by one monovalent (M^+) and one trivalent (M^{3+}) cation, consequently maintaining the overall neutrality of the crystal. Thus a new class of materials with composition $A_2M^+M^{3+}X_6$, named doubled perovskites (DPs), was developed that exhibits 3D perovskite structure and also maintains crystal neutrality.[15,16] Historically, such kind of materials have been previously investigated as ferroelectric in the 1960s under the name "elpasolites" with numerous compositions $A_2M^+M^{3+}X_6$ (here A and M^+ = Na^+, K^+, Li^+, Rb^+, Cs^+, Tl^+, Ag^+ *etc.*; M^{3+} = Fe^{3+}, Al^{3+}, Bi^{3+}, Ln^{3+}, Ga^{3+}, *etc.*; X = Cl^{1-}, Br^{1-}, F^{1-}, I^{1-}).[17–19]

Currently, two potential members of the DP family, $Cs_2AgBiBr_6$ and $Cs_2AgBiCl_6$, have been suggested owing to their promising air-exposed stability and photovoltaic (PV) uses.[20–27] These materials, on the other hand, exhibit weak photoluminescence (PL) output as well as low efficiency of power

[a]*Department of Physics, RIPHAH International University, Campus Lahore, Pakistan. E-mail: naveedcssp@gmail.com*

[b]*Institute of Physics, The Islamia University of Bahawalpur, Bahawalpur 63100, Pakistan*

[c]*Electrical and Biological Physics, Krangwoon University, Seoul, 01897, South Korea*

[d]*Plant Production Department, College of Food and Agriculture Sciences, King Saud University, P. O. Box 2460, Riyadh 11451, Saudi Arabia*

conversion (2.2%) for photovoltaic device applications that are attributed to their indirect band-gap.[28] Therefore, current investigations are focused on direct band-gap DP systems as an alternate potential choice.[29–33] Computational studies regarding various $A–M^{+}–M^{3+}–X$ compositions have anticipated diverse stable DPs, such as Cs_2AgInX_6, Rb_2AgInX_6, and Rb_2CuInX_6 ($X = Cl^{1-}$, Br^{1-}), that essentially show a direct band-gap across the entire spectral range essential regarding conversion of solar energy (*i.e.* 1.5–2.5 eV).[34,35] After Volonakis *et al.*'s groundbreaking breakthrough in 2016,[8] the synthesis of bulk $Cs_2AgInCl_6$ perovskite material was reported by various investigators which exhibits a DP structure at room temperature and belongs to the space group $Fm\bar{3}m$. Moreover, the said material also shows a fundamental direct band-gap of about 2 eV (described range 2.1–2.6 eV), extended carrier lifetime (6 s), and excellent stability (regarding heat, light, and moisture), making it a possible substitute for Pb-based halide perovskites.[36–39] Through the use of DFT calculations, it has been found that the material $Cs_2AgInCl_6$ exhibits a flat valence band maximum (VBM) that is primarily determined by Ag-4d orbitals and Cl-3p orbitals, and a dispersive conduction band minimum (CBM) originated from the delocalized 5s states.[36]

Moreover, the energy needed for the transition of photogenerated carriers is decreased by the direct transport pathway in $Cs_2InAgCl_6$, which improves the polycarboxylate superplasticizer (PCE). Nevertheless, even though films with a stable double perovskite structure were successfully synthesized in the $Fm\bar{3}m$ space group, the PBE method's estimated gap values of 2.9–3.3 eV became challenging for the photovoltaic application of $Cs_2InAgCl_6$ compound. While the broad band-gap problem may be resolved by using a BrCl solution, it should be noted that the synthesis of $Cs_2InAgBr_6$ became a difficult task partly because bromine speeds up the compound's instability.[39] From this angle, it can be perceived that the field of double perovskites for solar applications is noticeably lacking in practical solutions thus prompting us to investigate other constituents.[40–43] The material's remarkable stability and comparatively large bandgap energy (E_{gopt}) were the driving force for Nandha *et al.*'s work comprising the addition of Mn^{2+} cations to $Cs_2AgInCl_6$ powders in order to improve the optical properties of substituted compound.[38] The most extensively studied tactic for doping II–VI semiconductors and halide perovskite nano-crystals (NCs)[44,45] has been the incorporation of Mn into a wide band-gap semiconductor host lattice.[45] These systems produce d–d orbital emission (yellow–orange) because the photo-excited host lattice efficiently transfers its energy to manganese (Mn) ions, which in turn facilitates electronic transitions within d-orbitals. Such color-centered impurities, namely Mn^{2+} ions, give rise to photoluminescence (PL) with striking characteristics including prolonged lifetimes, substantial PL quantum yield (QY) as well as a significant Stokes shift that consequently reduces the possibility of self-absorption in the system.[46–49] Orange emission was detected at approximately 630 nm in Mn-substituted $Cs_2AgInCl_6$ powders (at Mn^{2+} concentration = 0.9%) having PLQY of almost 3–5%, consequently making it an attractive lead-free DP.[38]

Consistent with our extensive literature exploration, a comprehensive analysis regarding structural, electrical, and magnetic investigations of Mn-substituted $Cs_2AgInCl/Br_6$ FM double perovskites is still unreported. Furthermore, DFT computations related to the thermoelectric characteristics of Mn-substituted $Cs_2AgInCl/Br_6$ DPs are also unreported in the published literature. This research article designates the outcomes regarding DFT simulations to investigate the structural, electronic, elastic, magnetic, and thermoelectric characteristics of Mn-substituted $Cs_2AgInCl/Br_6$ dual perovskites with a particular emphasis on the 25% Mn content.

2. Computational scheme

Ab initio modeling is a widely employed approach for investigating materials titled for cutting-edge device applications. To investigate the existence of a stable FM semiconducting ground state within Mn-substituted $Cs_2AgInCl/Br_6$ dual perovskites, we have worked with FP-LAPW+lo approach, incorporated within the Wein2k software,[50] and originated from spin-polarized DFT. Using the PBEsol generalized gradient approximation, the structural and electronic properties are computed, and the Kohn–Sham orbitals are evaluated in a self-consistent mode.[51] Precise electrical and optical features are determined, using the newly presented modified Becke–Johnson (mBJ) functional,[52] revealing remarkable consistency with experimental findings.[53] The band gap computed using the modified Becke–Johnson (mBJ) functional was found closely consistent with experimental outcomes that in turn outclass the already used functionals. Already published article[52] offers a complete comparative analysis of band gap calculations performed by employing different methods, revealing the dominance of mBJ functional with respect to accuracy.

Using a $1 \times 1 \times 1$ supercell, the pure $Cs_2AgInCl/Br_6$ and substituted $Cs_2AgIn_{1-x}Mn_xCl/Br_6$ ($x = 0.25$) binary perovskites having space group $Fm\bar{3}m$ (cubic) are probed at room temperature (see Fig. 1(a) and (b)). Fig. 1(b) depicts that the substituted DPs exhibited the existence of $Fm\bar{3}m$ space group at substitution level $x = 0.25$. To facilitate subsequent computations, PBEsol-GGA functional is employed to optimize the experimentally measured lattice parameters.

The cut-off parameter was determined by multiplying the maximum plane wave vector (K_{max}) and the muffin-tin sphere's radius was set at 8. Additionally, utilizing $G_{max} = 18$ a.u.$^{-1}$, the potential inside the interstitial void is computed. The values of Muffin-tin radii regarding Cs, Ag, Mn, Cl, and Br atoms were used as 2.45 (a.u.), 2.40 (a.u.), 2.35 (a.u.), 2.21 (a.u.) and 2.25 (a.u.), respectively. A $10 \times 10 \times 10$ k-mesh is used for the integration of the Brillouin zone. The charge and total energy were allowed for preferable convergence to values 10^{-3} e and 10^{-4} Ry, respectively. We employed the BoltzTraP software[54] which is customized for the electronic structure of Mn-substituted $Cs_2AgInCl/Br_6$ DPs, to study the transport properties effectively. It is important to remember that a higher-level selection of k points was carried out for all BoltzTrap computations. Finally, the parameters such as electrical conductivity (σ), thermal conductivity (κ), Seebeck coefficient (S), and power factor were studied within the temperature range (200–800 K).

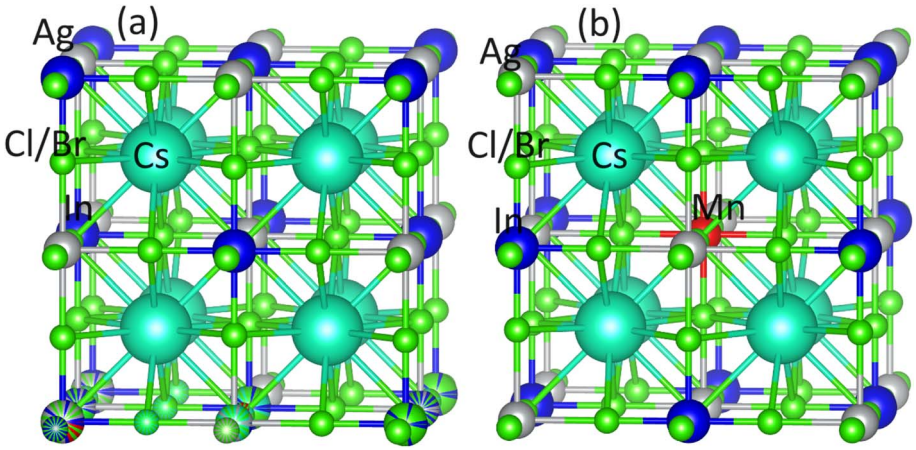

Fig. 1 The crystal structure for (a) NM $Cs_2AgInCl/Br_6$, (b) FM $Cs_2AgIn_{0.75}Mn_{0.25}Cl/Br_6$.

3. Results and discussions

3.1 Structural and elastic properties

For all the four investigated materials [$Cs_2AgIn_{1-x}Mn_xCl_6$ (x = 0.00, 0.25), $Cs_2AgIn_{1-x}Mn_xBr_6$ (x = 0.00, 0.25)], the optimized lattice parameters (a) and bulk moduli (B), presented in Table 1, are obtained by optimization and fitting of the computed volume and energy with well-known Birch–Murnghan equation.[55]

Table 1 The calculated lattice parameters, bulk modulus values, energy differences and Curie temperature (T_C) of $Cs_2AgIn_{1-x}Mn_xCl/Br_6$ (x = 0.00, 0.25)

	a_0 (Å)	B_0 (GPa)	$\Delta E_1 = E_{NM} - E_{FM}$	T_C (K)
$Cs_2AgInCl_6$	10.41	38.84	—	—
Exp.	10.48[a]			
$Cs_2AgIn_{0.75}Mn_{0.25}Cl_6$	10.42	35.80	4.56	770
$Cs_2AgInBr_6$	10.96	30.73	—	—
Exp.	11.00[b]			
$Cs_2AgIn_{0.75}Mn_{0.25}Br_6$	10.97	29.72	3.88	690

[a] Ref. 56. [b] Ref. 57.

Physically, bulk modulus indicates the crystal's hardness by elucidating the crystal's capacity to withstand deformations induced by uniform pressure. The validity of our computed results regarding lattice parameters and bulk moduli (Table 1) can be assessed by their complete agreement with previously published theoretical and experimental research articles.[56,57] An increase in lattice parameter (a) with enhancement in Mn content has been observed which is ascribed to a smaller ionic radius of Mn^{2+} (0.80 Å) compared with In^{2+} (0.81 Å). Moreover, a decrease in bulk modulus (B) with an increase of parameter (a) was observed which revealed the inverse relation of a with B.[58,59] Understanding the stability comparison between the nonmagnetic (NM) and ferromagnetic (FM) states was achieved by comparing the total energy of these states as estimated using the relation $\Delta E_1 = E_{NM} - E_{FM}$. The stability of the FM phase was

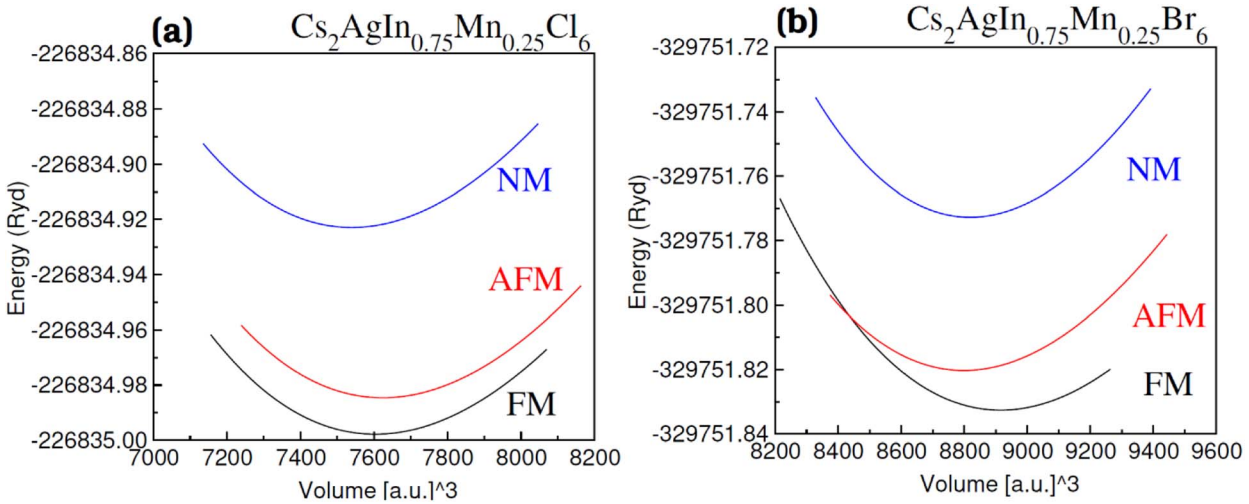

Fig. 2 Volume optimization plot of DPs (a) $Cs_2AgIn_{0.75}Mn_{0.25}Cl_6$ and (b) $Cs_2AgIn_{0.75}Mn_{0.25}Br_6$ in nonmagnetic (NM), antiferromagnetic (AFM) and ferromagnetic (FM) phase.

Table 2 Calculated elastic constant (C_{11}, C_{12}, C_{44}) for undoped and Mn-doped $Cs_2AgInCl/Br_6$ and their calculated bulk modulus (B_0), shear modulus (G), Young modulus (Y), Poisson's ratio (ν), Pugh ratio (B_0/G) and anisotropic (A) using PBEsol-GGA

	C_{11}	C_{12}	C_{44}	B_0	G	Y	B_0/G	ν	A
$Cs_2AgInCl_6$	89.44	11.18	14.08	37.26	21.51	54.12	1.73	0.26	0.36
$Cs_2AgIn_{0.75}Mn_{0.25}Cl_6$	55.28	24.01	28.55	34.43	22.42	55.26	1.54	0.23	0.31
$Cs_2AgInBr_6$	81.28	5.50	10.57	30.76	18.18	45.57	1.69	0.25	0.28
$Cs_2AgIn_{0.75}Mn_{0.25}Br_6$	57.52	11.48	16.23	26.82	18.67	45.47	1.44	0.22	0.24

validated through a positive value of ΔE_1 (see Fig. 2(a) and (b)) and their calculated FM $Cs_2AgIn_{0.75}Mn_{0.25}Cl/Br_6$ DPs are given in Table 1.

The orientation of magnetic moments is detailed for both ferromagnetic (FM) and anti-ferromagnetic (AFM) configurations within Mn-substituted $Cs_2AgInCl/Br_6$ DPs, with

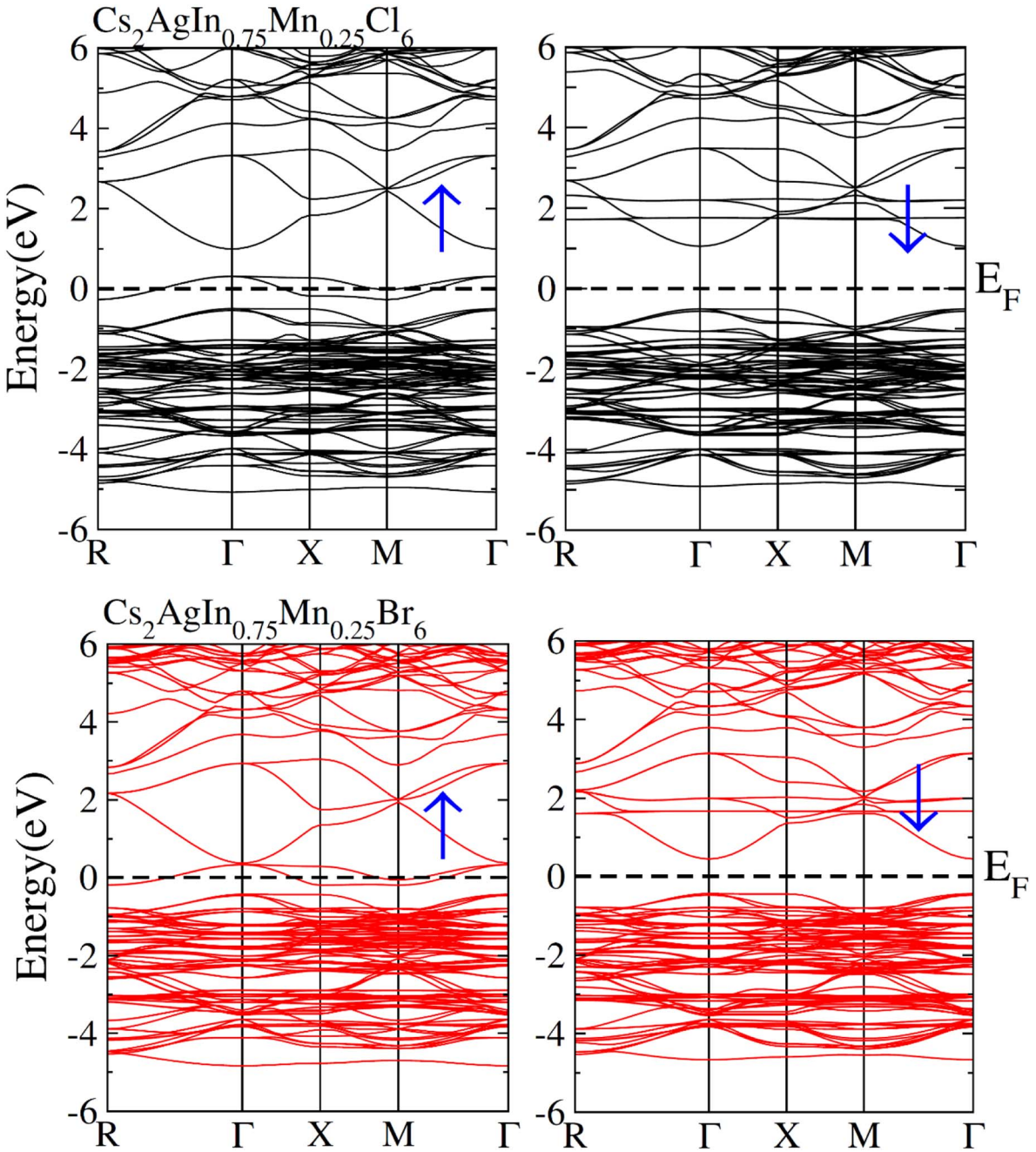

Fig. 3 Calculated spin polarized band structures plot for FM $Cs_2AgIn_{0.75}Mn_{0.25}Cl_6$ and (FM) $Cs_2AgIn_{0.75}Mn_{0.25}Br_6$.

a consistent arrangement of spins in antiparallel and parallel directions between Mn atoms. The magnetic interconnection among the two Mn atoms is expressed as energy difference among the AFM and FM structures $\Delta E = E_{FM} - E_{AFM}$. The energy values for Mn-substituted $Cs_2AgInCl/Br_6$ DPs compounds are recorded 2.24 eV and 1.85 eV respectively. It can be seen that the FM structure exhibits superior characteristics compared to the AFM states for all aspects. The Curie temperature (T_C) has been determined by employing smearing in mean-field approximations, expressed as $k_B T_C = \frac{2}{3}\Delta E$ and the Heisenberg model.[60] Table 1 shows the anticipated T_C values, aligning with the recently disclosed range of 600 to 1000 K.[61] The investigated Mn-substituted exhibit a notably high Curie temperature (T_C), which is ascribed to the substantial energy difference (ΔE) among the ferromagnetic (FM) and antiferromagnetic (AFM) states.

The computed elastic constants C_{ij} for undoped and Mn-doped $Cs_2AgInCl/Br_6$ are presented in Table 2. These computed elastic constants satisfy the mechanical stability criteria, specifically $(C_{11}-C_{12}) > 0$, $C_{11} > 0$, $C_{44} > 0$ and $C_{12} > 0$ which are typically for a cube crystal structure.[62] This adherence to the stability criteria is crucial when considering these materials for fabrication of devices. Additionally, the bulk modulus (B) has been determined using the formula $B = (C_{11} + 2C_{12})/3$ based on the calculated elastic constants[63] and the resulting values align well with the bulk modulus (B_0) estimates through volume optimization plot. The Poisson ratio (ν) with a value exceeding 0.26 and the Pugh ratio (B_0/G) surpassing 1.75 serve as matrices to distinguishing between brittle and ductile behavior of materials, as detailed in ref. 64. Table 1 shows that our materials exhibit brittle behavior as determined by the computed values of ν and B_0/G. Furthermore, anisotropy factor denoted as A and calculated by using the formula $A = 2C_{44}/(C_{11} - C_{12})$ represents another parameter characterizing the directional properties of the materials under examination. The unit value of A indicates isotropic materials whereas values greater or smaller than unity suggest anisotropic behavior. Clearly our material exhibits anisotropic properties.

3.2 Electronic studies

Fig. 3 depicts the computed band structures including spin polarization for $Cs_2AgIn_{1-x}Mn_xCl/Br_6$ ($x = 0.25$) using the optimized lattice constant. The precise investigations regarding the electronic characteristics of $Cs_2AgIn_{1-x}Mn_xCl/Br_6$ compounds were accomplished through well-known mBJ functional. Zero energy Fermi level was adopted as a reference point. It is obvious that the conduction band (CB) minima represent the direction of X-symmetry, while the valence band (VB) minima represent the direction of Γ-symmetry that traverses Fermi level in spin-up (↑) mode. Conversely, the symmetric position of CB minima and VB minima is noticed at Γ-symmetry direction in the spin-down (↓) channel as well as inside the Fermi level. The presence of the mentioned exchange mechanism in these materials led to an insulating bandgap. Therefore, one can say that Half Metallic Ferromagnets (HFM) comprise spin-down channel, insulating bandgap, and spin-up channel with a metallic character.

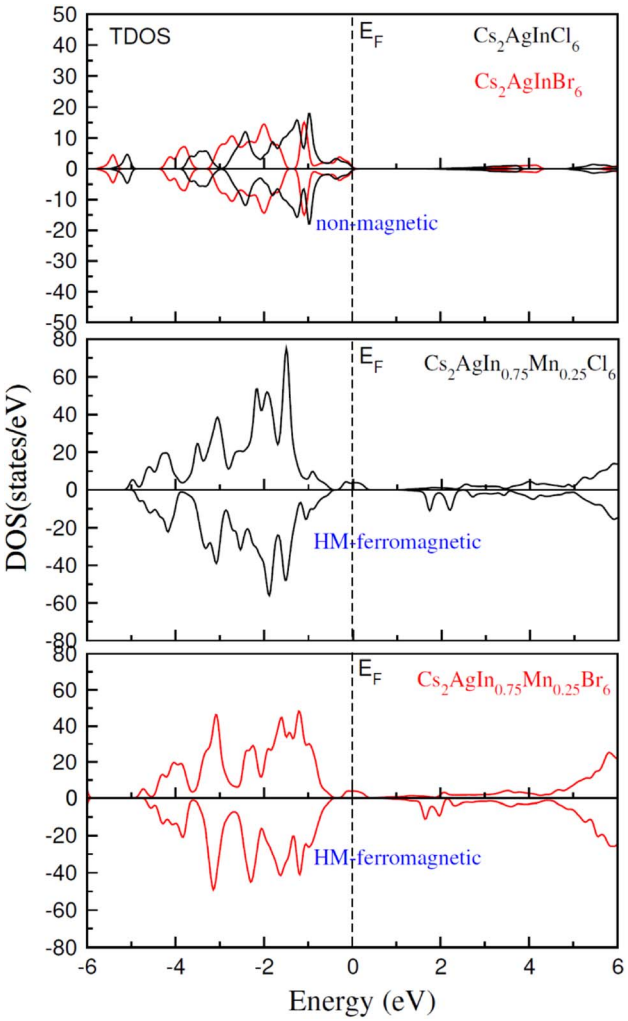

Fig. 4 Calculated TDOS plot for NM $Cs_2AgInCl/Br_6$ and FM $Cs_2AgIn_{0.75}Mn_{0.25}Cl/Br_6$.

Table 3 presents our calculated results regarding spin down bandgap revealing that investigated spinels show emissions in the visible portion of the electromagnetic spectrum, thus

Table 3 Calculated values of spin-down gap ($\downarrow E_g$ (eV)), half-metallic gap (g_h (eV)), local magnetic moments, and total magnetic moments per atom (in terms of μ_B) for $Cs_2AgIn_{0.75}Mn_{0.25}Cl/Br_6$

Doped DPs	$\downarrow E_g$ (eV)	g_h (eV)	μ_B (total)	μ_B (Mn)	μ_B (Cs)	μ_B (Ag)	μ_B (In)	μ_B (Cl/Br)
$Cs_2AgIn_{0.75}Mn_{0.25}Cl_6$	1.7	0.5	4.000	4.009	0.0003	−0.042	−0.002	0.0005
$Cs_2AgIn_{0.75}Mn_{0.25}Br_6$	1.0	0.4	4.000	4.015	0.0001	−0.027	−0.001	0.0006

suitable for solar cell applications. A similar trend has been observed for computed total density of states (TDOS) as depicted in Fig. 4–6. The calculations regarding TDOS and PDOS were executed to study exchange energies behavior and the HMF nature of materials. Spin polarizability (P) was calculated using DOS employing the following relation:[65]

$$P = \frac{N\downarrow E_F - N\uparrow E_F}{N\downarrow E_F + N\uparrow E_F} \times 100$$

the symbols (↓) and (↑) denote TDOS for spin-down and spin-up channels, respectively. Using the aforementioned relation, P has the predicted value of 100% thus designating Mn-doped DPs ($Cs_2AgInCl/Br_6$) as a prospective material for spintronic devices.

TDOS and PDOS illustrated in Fig. 4–6 were computed using modified Becke–Johnson (mBJ) potential and correspondingly describe the atomic plus orbital level configuration of different band states. For un-substituted materials ($Cs_2AgInCl/Br_6$) complete absence of spin-splitting between spin (↑) and spin (↓) states has been observed as depicted in Fig. 4(a). However, the substitution of Mn^{2+} ions triggered the spin-splitting process by simultaneous shifting of VBM towards E_f and CBM away from E_f towards the high energy terminal. But, for spin-down channel, a converse trend is observed as obvious in Fig. 4(b) and (c). Furthermore, the probability of exhibiting half-metallic nature can be disregarded, and it can be assumed that compounds display semiconducting properties as in both spin channels, no states are possible at E_f, and E_f lies inside the band gap. It is quite clear from PDOS plots, as demonstrated in Fig. 5 and 6, that the lower portion of VB, located at about −5 eV, is narrow and mostly contains Ag-d states having minor contributions from Cl/Br-s states. Hybridization of Mn-3d states with Ag-d and Cl/Br-p states constitute the upper portion of VB.

The replacement of In^{2+} ions with Mn^{2+} ions creates Mn-3d states that undergo a splitting process through the crystal field to yield doubly degenerated (e_g) and triply degenerated (t_{2g}) states. The semiconducting nature of compounds is also verified through the spin-flip approach describing the inevitable provision of band gap energy for an electron to jump from the majority band to the minority band. The origin of ferromagnetism can be elucidated through different methods including the Stoner model, Zener model (p–d hybridization), and double exchange. Our results do not support a half-metallic nature as the majority of d-band above VB remains below E_F. So, free carrier-mediated ferromagnetic interactions cannot be the probable cause of ferromagnetism. Therefore, the direct exchange interactions involving the hybridization of impurity d-states with Cl/Br p-states in spin-up and spin-down band

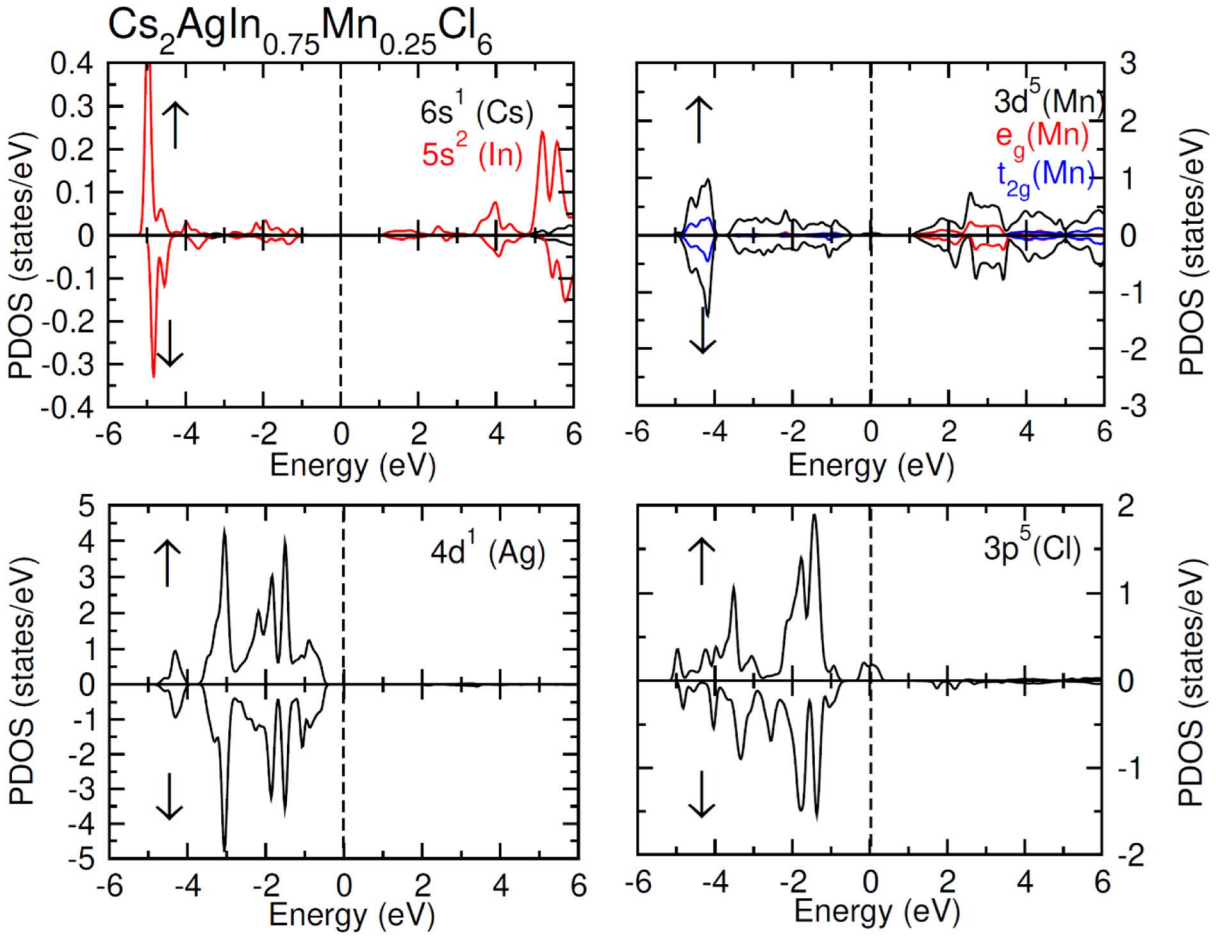

Fig. 5 Calculated PDOS plot of Cs, Ag, In, Mn and Cl atoms for FM $Cs_2AgIn_{0.75}Mn_{0.25}Cl_6$.

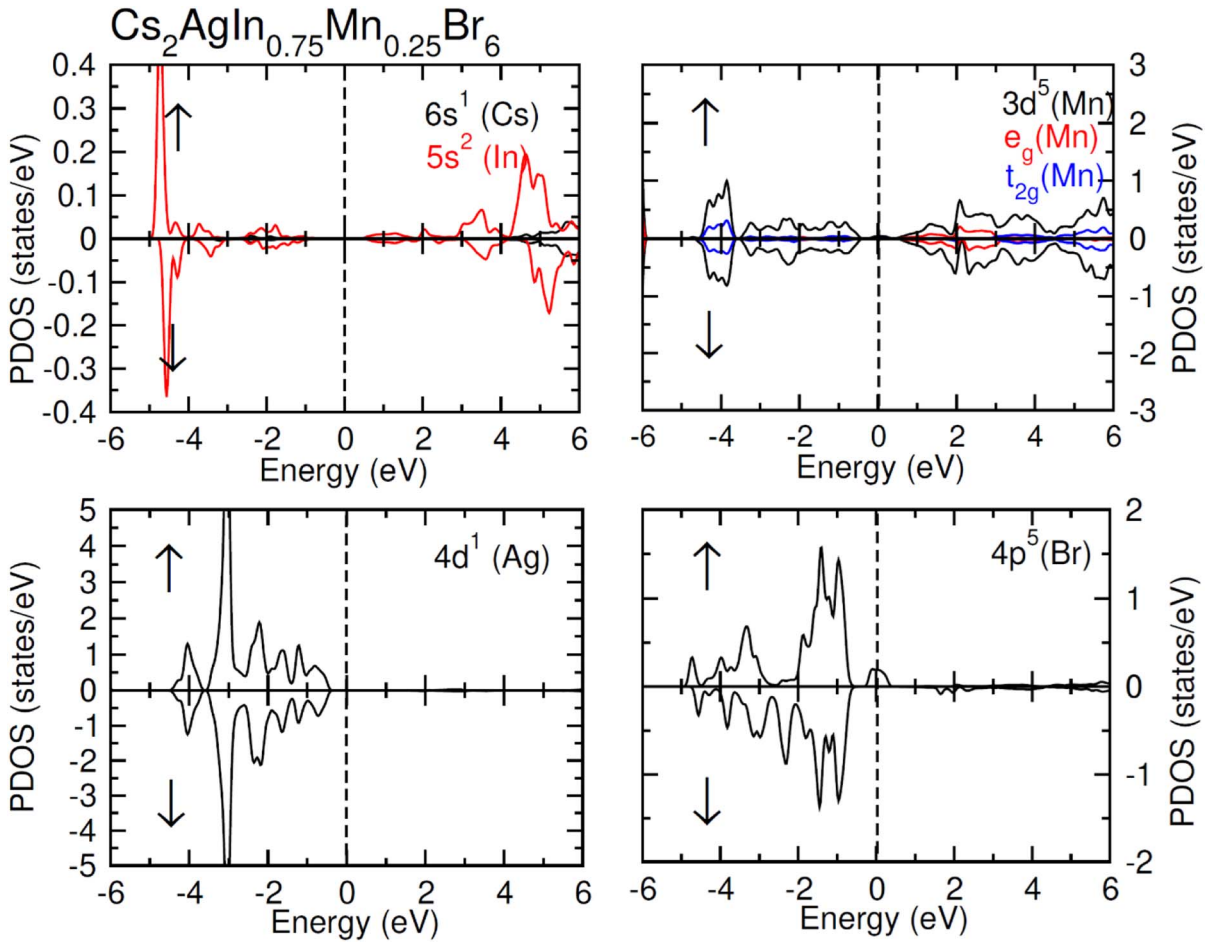

Fig. 6 Calculated PDOS plot of Cs, Ag, In, Mn and Cl atoms for FM $Cs_2AgIn_{0.75}Mn_{0.25}Cl_6$.

(exchange split) are considered as sources of ferromagnetism in investigated compounds as illustrated in Fig. 4. The partial DOS for $Cs_2AgIn_{0.75}Mn_{0.25}Cl_6$ exhibits distinct d-states in both spin channels and comparably sharp degenerated t_{2g} and e_g states (see Fig. 5), but in the case of $Cs_2AgIn_{0.75}Mn_{0.25}Br_6$ an increase in broadness and decrease in sharpness of both degenerated states has been identified (see Fig. 6).

3.3 Absorption spectra

Optical characteristics of Mn-doped $Cs_2AgInCl/Br_6$ have been investigated to explore potential applications in optoelectronics. The calculated absorption spectra against incident photon energy (0 to 10 eV) denoted as $\alpha(\omega)$ and depicted in Fig. 7, serves as a useful indicator of the materials absorbent properties. The energy range within which $\alpha(\omega)$ become negligible is indicative of the transparency of the materials to incident energy. The absorption edge is the critical threshold at which the absorption of intruding energy begins. The absorption edge of $Cs_2AgIn_{0.75}Mn_{0.25}Cl/Br_6$ is observed at 2.0 eV and 1.4 eV, respectively in the current study. Moreover, the difference between absorption edge and the calculated band gap can be clarified by the fact that we define the energy at which substantial absorption becomes clearly evident as the absorption edge, this not accounting for the minor absorptions linked to fundamental band gaps. The absorption exhibits a linear increase with energy after this edge point, culminating at a maximum point. Additionally, when the X-ions shift from Cl to Br and in $Cs_2AgIn_{0.75}Mn_{0.25}Cl/Br_6$, a red shift in the

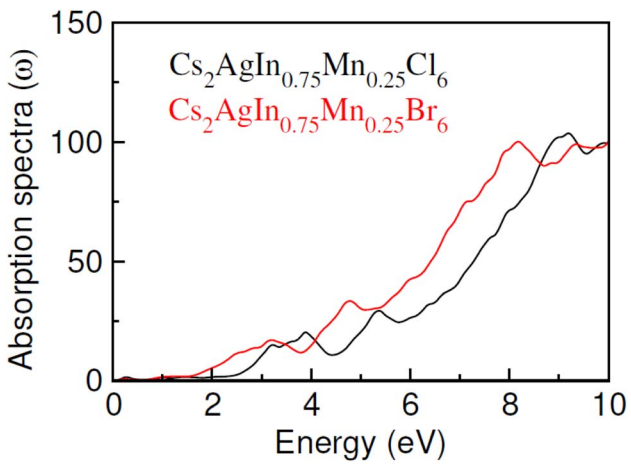

Fig. 7 The calculated absorption $\alpha(\omega)$ of $Cs_2AgIn_{0.75}Mn_{0.25}Cl/Br_6$ halides.

absorption edge is observed, accompanied by predominant absorption, which is a result of the widened energy band gap.

3.4 Magnetic studies

The ferromagnetic character of studied Mn substituted DPs ($Cs_2AgInCl/Br_6$) originated because the presence of magnetic substituted ions initiates strong exchange interactions between p-states of anions and d-states of substituted cations by way of p–d hybridization causing edge splitting of VB and CB. The Hamiltonian (H) in mean field theory (MFT) can be expressed in terms of cations content (N_0), p–d exchange factor (β), free hole spins (s), and Mn spins (S), as:[66,67]

$$H = -N_0\beta sS \quad (1)$$

Table 4 Computed crystal field energy (Δ_{CF}), exchange splitting Δ_x(d), p–d exchange constant ($N_0\beta$) and s–d exchange constant ($N_0\alpha$) for $Cs_2AgIn_{0.75}Mn_{0.25}Cl/Br_6$

Parameters	$Cs_2AgIn_{0.75}Mn_{0.25}Cl_6$	$Cs_2AgIn_{0.75}Mn_{0.25}Br_6$
E_{crys}	2.4	2.0
Δ_x(d)	6.4	5.8
Δ_x(pd)	−0.6	−0.5
$N_0\alpha$	0.7	0.5
$N_0\beta$	−0.30	−0.25

The above relation was employed to compute exchange constants $N_0\alpha$ and $N_0\beta$ that respectively account for the strength of s–d and p–d interactions that can be expressed as:

$$N_0\alpha = \frac{\Delta E_C}{x\langle S\rangle}, \text{ and } N_0\beta = \frac{\Delta E_V}{x\langle S\rangle} \quad (2)$$

The terms x and $\langle S\rangle$ symbolize the concentration and mean magnetic moment of Mn^{2+} ions. While ΔE_C and ΔE_V denote band edge splitting associated with CB and VB, respectively. The negative signs of computed exchange constants ($N_0\alpha$ and $N_0\beta$) reveal the ferromagnetic nature of s–d and p–d interactions. Moreover, ferromagnetism is favored by Mn-doped $Cs_2AgInCl/Br_6$ compounds owing to a greater magnitude of $N_0\beta$ compared to $N_0\alpha$. Further investigations regarding the ferromagnetic behavior of probed DPs were done through direct exchange constant Δ_x(d) deduced by the equation $\Delta_x(d) = d^{\downarrow} - d^{\uparrow}$ with the help of Fig. 5, and then compared with crystal field energy ($E_{crys} = d_{t_{2g}} - d_{e_g}$). One can deduce from Fig. 5 and Table 4 that $\Delta_x(d) \gg E_{crys}$ that in turn authenticate the vital role of E_{crys} in the band splitting procedure and hence stabilize the ferromagnetic state.

The measured value of the total magnetic moment was found to be 3 μ_B. The local magnetic moments of various ions present in the structure of studied compounds (*i.e.* Mn^{2+}, In^{3+}, Ag^{1+}, Cs^{+} and Cl^{1-}/Br^{1-}) are presented in Table 3. It can be seen

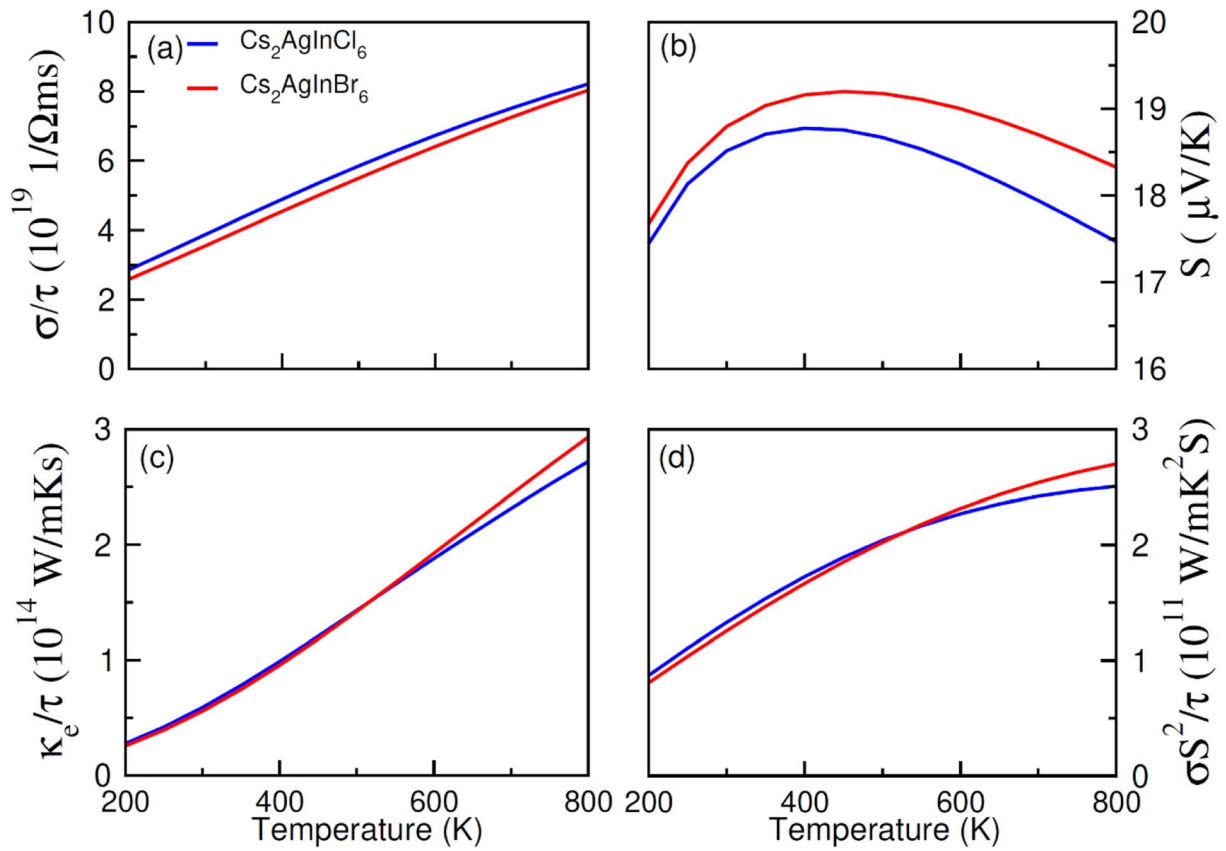

Fig. 8 The calculated (a) electrical (σ/τ), (b) Seebeck coefficient (S), (c) thermal (k_e/τ) conductivities, (d) and power factor for NM $Cs_2AgInCl/Br_6$ against temperatures (200 K–800 K).

that Mn^{2+} ions provide the main contribution to m_{total}, whereas a small contribution is furnished by In^{3+} and Cl/Br ions. The variations in the magnetic moment of (In, Cl/Br) sites at the expense of the magnetic moment of Mn sites were attributed to exchange interactions between Mn-3d and Cl/Br-p states. However, the presence of various exchange coupling among various lattice sites leads to the transfer of magnetic moments towards nonmagnetic sites.

3.5 Thermoelectric properties

The transport (electronic and thermoelectric) features of spin-polarized materials play a key role in designing spintronic and thermoelectric appliances.[68,69] Thermoelectric devices can convert heat into electrical energy using temperature divergence, and their efficiency can be determined through thermoelectric parameters including Seebeck coefficient (S), power factor ($\sigma S^2/\tau$), thermal (κ/τ) and electrical conductivity (σ/τ). The thermoelectric performance of $Cs_2AgIn_{1-x}Mn_xCl/Br_6$ ($x = 0.00$, 0.25) double perovskites have been studied for their promising use in thermoelectric devices. The calculated results regarding the mentioned thermoelectric parameters (S, $\sigma S^2/\tau$, κ/τ, σ/τ), within the temperature extent 200–800 K, are presented in Fig. 8a–d and 9a–d.

An increase in electrical conductivity takes place due to the charges' flow and it leads to a forward current. For $Cs_2AgIn_{1-x}Mn_xCl/Br_6$ ($x = 0.25$) ferromagnetic compounds, a decrease in σ/τ with a rise of temperature up to 800 K has been observed. However, the rate of increment of σ/τ for $Cs_2AgIn_{1-x}Mn_xCl_6$ ($x = 0.00$, 0.25) compounds remained comparatively smaller than $Cs_2AgIn_{1-x}Mn_xBr_6$ ($x = 0.00$, 0.25), that can be observed in Fig. 8a and 9a. The interactions of charge carriers with lattice vibrations in the form of phonon waves give rise to thermal conductivity (κ/τ). We have studied only the electronic part of thermal conductivity (κ_e/τ) due to deficiency associated with the BoltzTrap code as it is based on the classical transport model.

Thermal conductivity can be calculated by using the relation between the rate of heat flow and temperature gradient as described by Fourier law given by the relation: $q = -\kappa dT/dx$, here, q stands for heat transfer rate, dT/dx denotes temperature gradient, and κ is coefficient of κ_e/τ. It is found that for DPs $Cs_2AgIn_{1-x}Mn_xCl/Br_6$ ($x = 0.00$, 0.25) thermal conductivity increased gradually up to 800 K indicating the active and dynamic contribution of charge carriers for energy transportation during the whole temperature range. It is obvious from Fig. 8c and 9c that at 800 K $Cs_2AgIn_{1-x}Mn_xCl_6$ ($x = 0.0$, 0.25) compounds showed the lowest value of thermal conductivity but the highest value was observed for $Cs_2AgIn_{1-x}Mn_xBr_6$ ($x = 0.0$, 0.25) compounds. It is deduced from Weidman–Franz law ($LT = \kappa/\sigma$) that compounds exhibiting smaller $\kappa/\tau : \sigma/\tau$ ratio are considered as good for thermoelectric applications. The

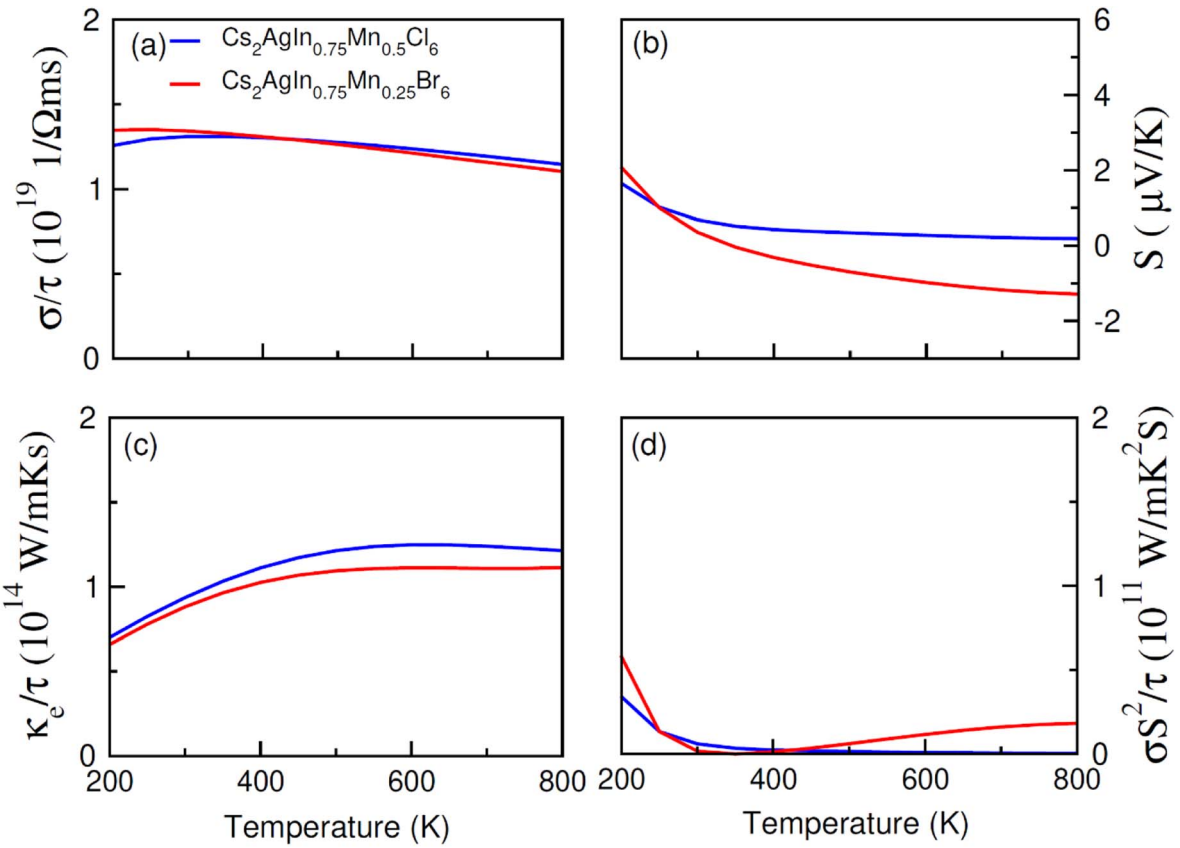

Fig. 9 The calculated (a) electrical (σ/τ), (b) Seebeck coefficient (S), (c) thermal (k_e/τ) conductivities, (d) and power factor for FM $Cs_2AgIn_{0.75}Mn_{0.25}Cl_6$ against temperatures (200–800 K).

computed ratio ($\kappa/\tau : \sigma/\tau$) for $Cs_2AgIn_{1-x}Mn_xCl/Br_6$ (x = 0.00, 0.25) compounds is about 10^{-6} revealing the capability of study materials to be utilized in thermoelectric devices.

To measure the temperature gradient, the Seebeck coefficient (S) between two incompatible metals was computed. The analysis of calculated S values (at 200 K) revealed that for $Cs_2AgIn_{1-x}Mn_xBr_6$ (x = 0.00, 0.25) compounds, the Seebeck coefficient is relatively small as compared to $Cs_2AgIn_{1-x}Mn_xCl_6$ (x = 0.00, 0.25) as depicted in Fig. 8b and 9b. For both series of DPs ($Cs_2AgIn_{1-x}Mn_xCl_6$ and $Cs_2AgIn_{1-x}Mn_xBr_6$) investigations also showed the convergence of S at 250 K and then divergence was observed up to 800 K. Furthermore, the maximum S value was found for $Cs_2AgIn_{1-x}Mn_xBr_6$ (x = 0.00, 0.25), while the minimum was realized for $Cs_2AgIn_{1-x}Mn_xCl_6$ (x = 0.00, 0.25). Additionally, the observation regarding the negative Seebeck coefficient for both DP series exhibits their n-type behavior.

Power factor ($S^2\sigma/\tau$) may be used to deduce thermoelectric efficiency; however, because thermal conductivity is not taken into account, the calculated values may be overestimated. However, our discussed results showed accurate trends in this regard. For both compounds, $Cs_2AgIn_{1-x}Mn_xCl/Br_6$ (x = 0.25), the value of power factor showed an increasing tendency up to 400 K and decreased afterward as depicted in Fig. 9d. The observed decrease in power factor at higher temperatures can be attributed to negative Seebeck coefficient (S).

4. Conclusion

This study was mainly focused on clarifying the physical properties of $Cs_2AgIn_{1-x}Mn_xCl/Br_6$ double perovskite materials with specific Mn contents (*i.e.* x = 0.00, 0.25). We used the Wien2k and BoltzTraP software to investigate the electrical transport and ferromagnetic behavior of these DPs. Optimization process revealed that the FM state exhibits maximum free energy compared to NM and AFM states. Calculated values of Curie temperature of Mn contents exhibit a notably high Curie temperature (T_C). It was observed that Mn substitution led to a decrease in B_0 and an increase of a_0 in the FM phase. Interestingly, our calculated values of a_0 for un-substituted DPs ($Cs_2AgInCl/Br_6$) agree quite well with experimental values. These computed elastic constants satisfy the mechanical stability criteria and materials exhibit brittle behavior as determined by the computed values of ν and B_0/G. Additionally, DOS studies and spin-polarized band structure analysis designated the half-metallic ferromagnetic character of the studied DPs. Analysis of the density of states (PDOS and TDOS) for $Cs_2AgIn_{1-x}Mn_xCl/Br_6$ (x = 0.25) yielded exchange interactions, and strong hybridization validated the ferromagnetic nature caused by electronic spin. Moreover, the difference between absorption edge and the calculated band gap can be justified. Furthermore, our computed exchange energy values revealed a higher direct energy (Δ_x(d)) value compared to the indirect energy (Δ_x(pd)) value, which consequently support the ferromagnetism. Moreover, it was noticed that the decrease in energy associated with the spin-down channel was attributed to $N_0\beta$ as well as to the observed red shift in Δ_x(pd). Notably, the DPs $Cs_2AgInCl/Br_6$ revealed higher thermoelectric conductivity values compared to $Cs_2AgIn_{1-x}Mn_xCl/Br_6$ (x = 0.25), as inferred from measurements of the κ/σ ratio and the power factor.

Conflicts of interest

There are no conflicts to declare.

Acknowledgements

The authors would like to thank Researchers Supporting Project number (RSP2024R118), King Saud University, Riyadh, Saudi Arabia.

References

1 Q. A. Akkerman, G. Rainò, M. V. Kovalenko and L. Manna, *Nat. Mater.*, 2018, **17**, 394–405.
2 M. Saliba, T. Matsui, J.-Y. Seo, K. Domanski, J.-P. Correa-Baena, M. K. Nazeeruddin, S. M. Zakeeruddin, W. Tress, A. Abate, A. Hagfeldt and M. Gratzel, *Energy Environ. Sci.*, 2016, **9**, 1989–1997.
3 C. N. Savory, A. Walsh and D. O. Scanlon, *ACS Energy Lett.*, 2016, **1**, 949–955.
4 Z. Huang, P. Luo, S. Jia, H. Zheng and Z. Lyu, *J. Phys. Chem. Solids*, 2022, **167**, 110746.
5 S. Mu, Q. Liu, P. Kidkhunthod, X. Zhou, W. Wang and Y. Tang, *Nat. Sci. Rev.*, 2020, **8**, 178.
6 Z. Deng, F. Wei, S. Sun, G. Kieslich, A. K. Cheetham and P. D. Bristowe, *J. Mater. Chem. A*, 2016, **4**, 12025–12029.
7 Z. Huang, P. Luo, Q. Wu and H. Zheng, *J. Phys. Chem. Solids*, 2022, **161**, 110479.
8 G. Volonakis, M. R. Filip, A. A. Haghighirad, N. Sakai, B. Wenger, H. J. Snaith and F. Giustino, *J. Phys. Chem. Lett.*, 2016, **7**, 1254–1259.
9 X. Li, S. Aftab, S. Hussain, F. Kabir, A. M. A. Henaish, A. G. Al-Sehemi and G. Koyyada, Dimensional diversity (0D, 1D, 2D, and 3D) in perovskite solar cells: exploring the potential of mixed-dimensional integrations, *J. Mater. Chem. A*, 2024, **12**, 4421–4440.
10 L. K. Ono, E. J. Juarez-Perez and Y. Qi, *ACS Appl. Mater. Interfaces*, 2017, **9**, 30197–30246.
11 A. Wang, X. Yan, M. Zhang, S. Sun, M. Yang, W. Shen, X. Pan, P. Wang and Z. Deng, *Chem. Mater.*, 2016, **28**, 8132–8140.
12 J. Guo, B. He, Y. Han, H. Liu, J. Han, X. Ma, J. Wang, W. Gao and W. Lü, *Nano Lett.*, 2024, **24**, 1114–1121.
13 J. Zhang, Y. Yang, H. Deng, U. Farooq, X. Yang, J. Khan, J. Tang and H. Song, *ACS Nano*, 2017, **11**, 9294–9302.
14 S. Fu, H. Wu, W. He, Q. Li, C. Shan, J. Wang and C. Hu, Conversion of Dielectric Surface Effect into Volume Effect for High Output Energy, *Adv. Mater.*, 2023, **35**, 2302954.
15 T. C. Jellicoe, J. M. Richter, H. F. J. Glass, M. Tabachnyk, R. Brady, S. E. Dutton, A. Rao, R. H. Friend, D. Credgington, N. C. Greenham and M. L. Böhm, *J. Am. Chem. Soc.*, 2016, **138**, 2941−−2944.
16 X.-G. Zhao, J.-H. Yang, Y. Fu, D. Yang, Q. Xu, L. Yu, S.-H. Wei and L. Zhang, *J. Am. Chem. Soc.*, 2017, **139**, 2630–2638.

17 L. R. Morss, M. Siegal, L. Stenger and N. Edelstein, *Inorg. Chem.*, 1970, **9**, 1771–1775.
18 F. Wei, Z. Deng, S. Sun, F. Xie, G. Kieslich, D. M. Evans, M. A. Carpenter, P. D. Bristowe and A. K. Cheetham, *Mater. Horiz.*, 2016, **3**, 328–332.
19 Z. Deng, F. Wei, F. Brivio, Y. Wu, S. Sun, P. D. Bristowe and A. K. Cheetham, *J. Phys. Chem. Lett.*, 2017, **8**, 5015–5020.
20 A. H. Slavney, T. Hu, A. M. Lindenberg and H. I. Karunadasa, *J. Am. Chem. Soc.*, 2016, **138**, 2138–2141.
21 E. T. McClure, M. R. Ball, W. Windl and P. M. Woodward, *Chem. Mater.*, 2016, **28**, 1348–1354.
22 M. R. Filip, S. Hillman, A. A. Haghighirad, H. J. Snaith and F. Giustino, *J. Phys. Chem. Lett.*, 2016, **7**, 2579–2585.
23 Z. Huang, Y. Zhang, H. Wang and J. Li, *Appl. Phys. Lett.*, 2023, **123**, 103501.
24 Y. Bekenstein, J. C. Dahl, J. Huang, W. T. Osowiecki, J. K. Swabeck, E. M. Chan, P. Yang and A. P. Alivisatos, *Nano Lett.*, 2018, **18**, 3502–3508.
25 X. Zhang, Y. Tang, F. Zhang and C. Lee, *Adv. Energy Mater.*, 2016, **6**, 1502588.
26 B. Yang, *et al.*, *Angew. Chem., Int. Ed.*, 2018, **57**, 5359–5363.
27 M. Wang, C. Jiang, S. Zhang, X. Song, Y. Tang and H. Cheng, Reversible calcium alloying enables a practical room-temperature rechargeable calcium-ion battery with a high discharge voltage, *Nat. Chem.*, 2018, **10**, 667–672.
28 W. Gao, *et al.*, *ChemPhysChem*, 2018, **19**, 1696–1700.
29 H.-J. Feng, W. Deng, K. Yang, J. Huang and X. C. Zeng, *J. Phys. Chem. C*, 2017, **121**, 4471–4480.
30 W. Meng, X. Wang, Z. Xiao, J. Wang, D. B. Mitzi and Y. J. Yan, *Phys. Chem. Lett.*, 2017, **8**, 2999–3007.
31 S. Ye, J. Zhu, S. Zhu, Y. Zhao, M. Li, Z. Huang and J. He, Design Strategies for Perovskite-Type High-Entropy Oxides with Applications in Optics, *ACS Appl. Mater. Interfaces*, 2023, **15**, 47475–47486.
32 L.-Z. Lei, Z.-F. Shi, Y. Li, Z.-Z. Ma, F. Zhang, T.-T. Xu, Y.-T. Tian, D. Wu, X.-J. Li and G.-T. Du, *J. Mater. Chem. C*, 2018, **6**, 7982–7988.
33 Y. Zhao, J. Jing, L. Chen, F. Xu and H. Hou, Current Research Status of Interface of Ceramic-Metal Laminated Composite Material for Armor Protection, *Acta Metall. Sin.*, 2021, **57**, 1107–1125.
34 A. Jain, O. Voznyy and E. H. Sargent, *J. Phys. Chem. C*, 2017, **121**, 7183–7187.
35 X.-G. Zhao, D. Yang, Y. Sun, T. Li, L. Zhang, L. Yu and A. Zunger, *J. Am. Chem. Soc.*, 2017, **139**, 6718–6725.
36 R. Yang, W. Yao, L. Zhou, F. Zhang, Y. Zheng, C. Lee and Y. Tang, Secondary Amines Functionalized Organocatalytic Iodine Redox for High-Performance Aqueous Dual-Ion Batteries, *Adv. Mater.*, 2024, 2314247.
37 J. Luo, S. Li, H. Wu, Y. Zhou, Y. Li, J. Liu, J. Li, K. Li, F. Yi, G. Niu and J. Tang, *ACS Photonics*, 2018, **5**, 398–405.
38 S. Guan, J. Zhou, S. Sun, Q. Peng, X. Guo, B. Liu and Y. Tang, *Adv. Funct. Mater.*, 2024, 2314890.
39 T. Wei, Y. Zhou, C. Sun, X. Guo, S. Xu, D. Chen and Y. Tang, *Nano Res.*, 2023, 1–7.
40 A. De, N. Mondal and A. Samanta, *Nanoscale*, 2017, **9**, 16722–16727.
41 R. Buonsanti and D. Milliron, *J. Chem. Mater.*, 2013, **25**, 1305–1317.
42 A. K. Guria, S. K. Dutta, S. D. Adhikari and N. Pradhan, *ACS Energy Lett.*, 2017, **2**, 1014–1021.
43 H. Yang, S. Santra and P. H. Holloway, *J. Nanosci. Nanotechnol.*, 2005, **5**, 1364–1375.
44 K. Xu and A. Meijerink, *Chem. Mater.*, 2018, **30**, 5346–5352.
45 C. Jiang, Z. Deng, B. Liu, J. Li, Z. Han, Y. Ma and Y. Ma, *ACS Photonics*, 2022, **9**, 3089–3093.
46 R. N. Bhargava, D. Gallagher, X. Hong and A. Nurmikko, *Phys. Rev. Lett.*, 1994, **72**, 416–419.
47 T. Xin, S. Tang, F. Ji, L. Cui, B. He, X. Lin and M. Ferry, *Acta Mater.*, 2022, **239**, 118248.
48 A. Nag, S. Chakraborty and D. D. Sarma, *J. Am. Chem. Soc.*, 2008, **130**, 10605–10611.
49 X. Chen and T. Yu, *Molecules*, 2023, **28**, 8087.
50 P. Blaha, K. Schwarz, G. Madsen, D. Kvasnicka and J. Luitz, *An Augmented Plane Wave Plus Local Orbital Program for Calculating Crystal Properties*, Vienna University of Technology, Vienna, Austria, 2001.
51 Z. Wu and E. R. Cohen, *Phys. Rev. B: Condens. Matter Mater. Phys.*, 2006, **73**, 235116.
52 F. Tran and P. Blaha, *Phys. Rev. Lett.*, 2009, **102**, 226401.
53 X. Chen, *Inorganics*, 2023, **11**, 215.
54 G. K. Madsen and D. J. Singh, *Comput. Phys. Commun.*, 2006, **175**, 67.
55 F. Murnaghan, *Proc. Natl. Acad. Sci.*, 1944, **30**, 244–247.
56 G. Xing, N. Mathews, S. Sun, S. S. Lim, Y. M. Lam, M. Grätzel, S. Mhaisalkar and T. C. Sum, *Science*, 2013, **342**, 344.
57 Y. Liu, I. J. Cleveland, M. N. Tran and E. S. Aydil, *J. Phys. Chem. Lett.*, 2023, **14**(12), 3000–3006.
58 P. K. Lam, M. L. Cohen and G. Martinez, *Phys. Rev. B: Condens. Matter Mater. Phys.*, 1987, **35**, 9190.
59 S. D. Reddy, M. Reddy, N. Raok, K. Gunasekhar and S. P. Reddy, *J. Optoelectron. Adv. Mater.*, 2007, **9**, 3743–3746.
60 G. S. Rushbrooke and P. J. Wood, On the Curie points and high temperature susceptibilities of Heisenberg model ferromagnetics, *Mol. Phys.*, 1958, **1**, 257–283.
61 B. Cai, X. Chen, M. Xie, S. Zhang, X. Liu, J. Yang, W. Zhou, S. Guo and H. Zeng, A class of Pb-free double perovskite halide semiconductors with intrinsic ferromagnetism, large spin splitting and high Curie temperature, *Mater. Horiz.*, 2018, **5**, 961–968.
62 M. Mattesini, R. Ahuja and B. Johansson, Cubic Hf3N4 and Zr3N4: a class of hard materials, *Phys. Rev. B: Condens. Matter Mater. Phys.*, 2003, **68**(18), 184108.
63 N. Wang, W.-Y. Yu, B.-Y. Tang, L.-M. Peng and W.-J. Ding, Structural and mechanical properties of Mg17Al12 and Mg24Y5 from first-principles calculations, *J. Phys. D Appl. Phys.*, 2008, **41**(19), 195408.
64 W. Voigt, Reprinted (1928) with an additional appendix, Leipzig, Teubner, New York, Johnson Reprint, 1966.
65 T. T. Q. Hoa, N. D. The, S. McVitie, N. H. Nam, L. V. Vu, T. D. Canh and N. N. Long, *Opt. Mater.*, 2011, **33**, 308–314.
66 B. Yang, H. Wang, M. Zhang, F. Jia, Y. Liu and Z. Lu, *Chem. Eng. J.*, 2023, **476**, 146834.

67 Z.-Z. Luo, S. Cai, S. Hao, T. P. Bailey, Y. Luo, W. Luo and Y. Yu, Extraordinary role of Zn in enhancing thermoelectric performance of Ga-doped n-type PbTe, *Energy Environ. Sci.*, 2022, **15**, 368–375.

68 M. Sajjad, Q. Mahmood, N. Singh and J. A. Larsson, Ultralow lattice thermal conductivity in double perovskite Cs2PtI6: a promising thermoelectric material, *Appl. Energy Mater.*, 2020, **3**(11), 11293–11299.

69 Y. Wang, J. Zhu, M. Li, G. Shao, H. Wang and R. Zhang, Thermal properties of high-entropy RE-disilicates controlled by high throughput composition design and optimization, *Mater. Des.*, 2023, **236**, 112485.